Journal of Computational Physics 233 (2013) 241–261

Contents lists available at SciVerse ScienceDirect

Journal of Computational Physics

journal homepage: www.elsevier.com/locate/jcp

A level set approach for diffusion and Stefan-type problems with Robin boundary conditions on quadtree/octree adaptive Cartesian grids

Joseph Papac [a,*], Asdis Helgadottir [b], Christian Ratsch [a], Frederic Gibou [b,c]

[a] Mathematics Department, University of California, Los Angeles, CA 91405, United States
[b] Mechanical Engineering Department, University of California, Santa Barbara, CA 93106, United States
[c] Computer Science Department, University of California, Santa Barbara, CA 93106, United States

ARTICLE INFO

Article history:
Received 22 November 2011
Received in revised form 24 August 2012
Accepted 25 August 2012
Available online 13 September 2012

Keywords:
Level set method
Epitaxial growth
Diffusion
Stefan problem
Sharp interface
Robin boundary condition

ABSTRACT

We present a numerical method for simulating diffusion dominated phenomena on irregular domains and free moving boundaries with Robin boundary conditions on quadtree/octree adaptive meshes. In particular, we use a hybrid finite-difference and finite-volume framework that combines the level-set finite difference discretization of Min and Gibou (2007) [13] with the treatment of Robin boundary conditions of Papac et al. (2010) [19] on uniform grids. We present numerical results in two and three spatial dimensions on the diffusion equation and on a Stefan-type problem. In addition, we present an application of this method to the case of the simulation of the Ehrlich–Schwoebel barrier in the context of epitaxial growth.

Published by Elsevier Inc.

1. Introduction

Diffusion and Stefan-type problems with Robin boundary conditions are of practical significance in a variety of fields. For example, these equations arise in heat transfer applications involving internal conduction and convection [11]; tissue imaging with near-infrared tomography [21]; and continuum models of epitaxial growth involving the Ehrlich–Schwoebel barrier [28] on step edges.

The mathematical formulation of a diffusion equation is as follows: consider a domain $\Omega = \Omega^+ \cup \Omega^-$ with boundary $\partial\Omega$, illustrated in Fig. 1, where the solution u satisfying the diffusion equation,

$$u_t = D\triangle u + g, \tag{1}$$

where D is the diffusion coefficient and g represents source terms, is to be solved in Ω^-. At the boundary of Ω^-, which we denote by Γ, a Robin boundary condition is imposed:

$$\nabla u \cdot \mathbf{n} + \alpha u = f, \quad \mathbf{x} \in \Gamma, \tag{2}$$

where $\mathbf{n}$ is the outward normal to Ω^-.

The mathematical formulation of the Stefan problem is a free boundary problem where the velocity of the free boundary is given by:

* Corresponding author. Tel.: +1 3102063570.
E-mail address: jepapac@gmail.com (J. Papac).

0021-9991/$ - see front matter Published by Elsevier Inc.
http://dx.doi.org/10.1016/j.jcp.2012.08.038

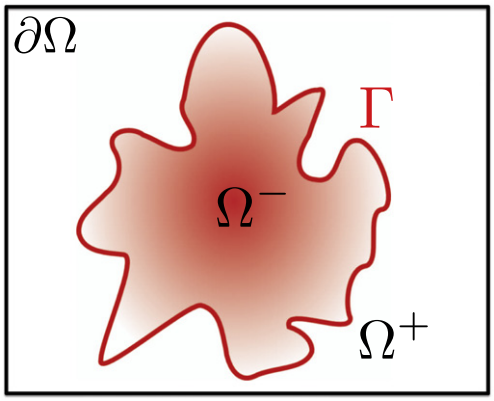

Fig. 1. A schematic of the level-set representation of the domain.

$$\mathbf{V} = [D\nabla u]_\Gamma, \tag{3}$$

where $[\cdot]_\Gamma$ denotes a jump across the interface. The phases on each side of the free boundary satisfy the diffusion equation (1) with boundary condition at the free boundary given by Eq. (2). The solution itself and the coefficients associated to each phase can be discontinuous across the interface.

A level-set approach to solving these equations on arbitrarily-shaped domains with uniform Cartesian grids was proposed in [19], where the treatment of the Robin boundary condition follows a finite volume approach [22,15]. The approach was introduced in two spatial dimensions and results in second-order accurate solutions for diffusion problems and first-order accurate solutions for Stefan-type problems. In this work, the numerical approach is extended to adaptive Cartesian grids in two and three spatial dimensions and we present an application to the simulation of the Ehrlich–Schwoebel barrier in the context of the island dynamics model of Caflisch et al. [4]. Some of the beneficial attributes of this approach are that it is straightforward to implement, computationally efficient, and geometrically robust so that complex interface topology and motion of sharp interfaces are handled implicitly.

2. Numerical approach

2.1. Level set method

In the case of Stefan-type problems, the evolution is driven by the physical interaction at the interface between phases. For this reason, it is desirable to have a sharp interface method, where the location of the interface can be precisely defined. In this work, we utilize the level-set method [18] for implicitly representing the moving interface. One well-documented limitation of the level-set method is its propensity for mass loss when the grid is too coarse, since the method is not intrinsically conservative. The discretization of these equations on non-graded adaptive grids allows for very fine resolution near the interface that significantly reduces mass loss while producing a computationally efficient method. A brief description of the level-set method follows and we refer the reader to [17,25] for more details.

Referring to the domain depicted in Fig. 1, we describe Ω^- by the set of points, $\mathbf{x}$, such that $\phi(\mathbf{x}) < 0$. Likewise, we describe Ω^+ by the set of points such that $\phi(\mathbf{x}) > 0$. The interface Γ is implicitly defined by the zero level set, $\phi(\mathbf{x}) = 0$. The evolution of the interface is then given by the evolution of the level-set function, ϕ, and obeys:

$$\phi_t + \mathbf{V} \cdot \nabla\phi = 0, \tag{4}$$

where $\mathbf{V}$ is an externally generated velocity field.

The outward unit normal to the interface, $\mathbf{n}$, and the interface mean curvature, κ, are calculated from the level-set function according to,

$$\mathbf{n} = \frac{\nabla\phi}{|\nabla\phi|} \quad \text{and} \quad \kappa = \nabla \cdot \mathbf{n},$$

respectively.

2.2. Structure of the adaptive Cartesian grid

We utilize non-graded Cartesian grids, those for which the size ratio between adjacent cells is unconstrained. The computational domain, Ω, is encompassed entirely within a root cell, a cube in three spatial dimensions or a square in two spatial dimensions, with grid nodes located at the vertices of the cell. The root cell is then recursively divided into equally-sized

sub-cells until the desired level of refinement is achieved, i.e. a parent cell is split into four child cells in two spatial dimensions and eight child cells in three spatial dimensions. This approach provides great flexibility in defining a suitable grid. In the simplest configuration, the domain can be divided into a standard uniform grid. The primary benefit, however, is the ability to locally refine as necessary to capture small-scale physical details, or to coarsen the grid in areas where the solution is smooth to reduce the computational cost.

While the criterion for refining the size of cells may be tailored specifically to the application at hand, in this work we have chosen a simple algorithm for generating the grid as proposed in [13,6], which is based on an estimate of the distance of each cell to the interface. More precisely, a cell is divided if the following condition is satisfied:

$$\min_{v \in \text{vertices}} |\phi(v)| < \text{Lip} \times \text{Diag}(C), \tag{5}$$

where $\phi(v)$ is the value of the level-set function at the vertices, v, of the grid cell, C. Lip is the Lipschitz constant, and $\text{Diag}(C)$ is the length of the diagonal of the cell. In our examples, we have chosen a value of $\text{Lip} = 1.1$ since our reinitialization algorithm produces level-set functions that are approximate signed distance functions. Additionally, we define two grid parameters, max level and min level that control the sizes of the largest and the smallest leaf cells in the domain: defining max level in a domain $[0,1]^2$ corresponds to setting $\Delta x = \Delta y = 1/2^{\text{max level}}$. Lastly, we impose a narrow band of uniform cells near the interface as a requirement for the discretization procedure. We do this by applying the criterion in (5) with the ϕ values increased by $\pm\Delta x$, $\pm 2\Delta x$, etc., where Δx is the size of the smallest cell's width.

The node-based Cartesian grid described above is well-suited for tree-based data structures; octree in three spatial dimensions and quadtree in two spatial dimensions. These data structures ease implementation by providing an efficient and straightforward way to access and store the data [23,24].

2.3. Approach for diffusion problems

Consider a diffusion equation (1) with boundary condition given by (2). We will utilize a discretization based on the Crank–Nicolson scheme in time. The spatial discretizations are given in the following sections.

2.3.1. Discretization in three spatial dimensions

We utilize a discretization in time based on the Crank–Nicolson scheme. When discretizing Eq. (1) in space and forming the associated linear system, we treat the grid nodes adjacent to the interface differently from the other nodes.

First, consider an octree grid node that is not adjacent to the interface. The most general case contains at most one two-dimensional T-junction and one three-dimensional T-junction, as depicted in Fig. 2. The value of the ghost node due to the two-dimensional T-junction is found by compensating the error of linear interpolation by the derivative in the transverse direction, as described in [13,5], and is given by,

$$u_2 = \frac{u_7 s_8 + u_8 s_7}{s_7 + s_8} - \frac{s_7 s_8}{s_3 + s_6}\left(\frac{u_6 - u_0}{s_6} + \frac{u_3 - u_0}{s_3}\right).$$

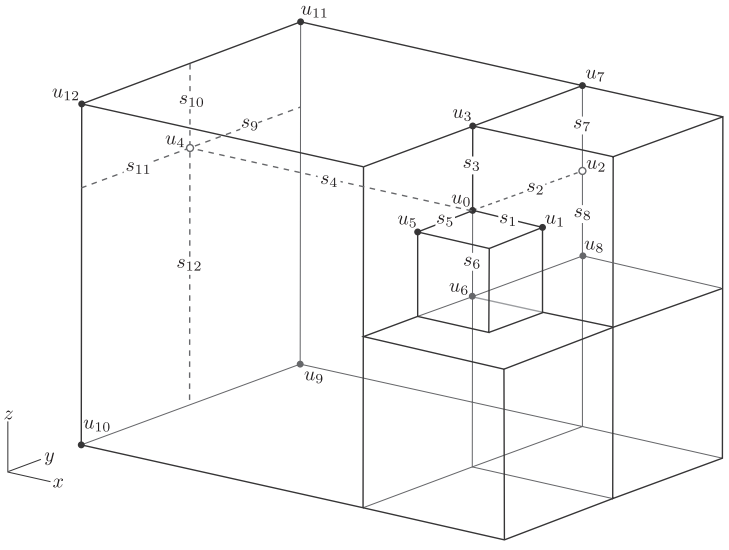

Fig. 2. Octree grid showing one two-dimensional T-junction node, u_2, and one three-dimensional T-junction node, u_4.

The value of the ghost node due to the three-dimensional T-junction is obtained similarly and is given by the following expression,

$$u_4 = \frac{s_{11}s_{12}u_{11} + s_{12}s_9u_{12} + s_{10}s_{11}u_9 + s_{10}s_9u_{10}}{(s_{10}+s_{12})(s_{11}+s_9)} - \frac{s_{10}s_{12}}{s_3+s_6}\left(\frac{u_3-u_0}{s_3}+\frac{u_6-u_0}{s_6}\right) - \frac{s_9s_{11}}{s_2+s_5}\left(\frac{u_2-u_0}{s_2}+\frac{u_5-u_0}{s_5}\right).$$

Once all of the necessary ghost nodes are defined, the first and second-order derivatives are calculated with the following formulas:

$$D_x^0 u_0 = \frac{u_4-u_0}{s_4}\cdot\frac{s_1}{s_1+s_4} + \frac{u_0-u_1}{s_1}\cdot\frac{s_4}{s_1+s_4}$$

and

$$D_{xx}^0 u_0 = \frac{u_4-u_0}{s_4}\cdot\frac{2}{s_1+s_4} - \frac{u_0-u_1}{s_1}\cdot\frac{2}{s_1+s_4},$$

and are used for constructing the linear system associated with the Crank–Nicolson time discretization of Eq. (1).

Next, consider the octree grid nodes near the interface. There are no T-junction nodes due to the uniform band of cells near the interface. We express the diffusion equation (1) in integral form,

$$\int_{\mathscr{C}\cap\Omega^-} u_t\,dV = b\int_{\mathscr{C}\cap\Omega^-}\nabla\cdot\nabla u\,dV + \int_{\mathscr{C}\cap\Omega^-} g\,dV,$$

where $\mathscr{C}$ is a fictitious finite volume cell defined around each octree node, as depicted in Fig. 3. The values of the level-set function are stored at the vertices of $\mathscr{C}$ and are found by averaging the nearest eight equidistant octree node values. Applying a Crank–Nicolson time discretization of Eq. (1), we obtain:

$$\int_{\mathscr{C}\cap\Omega^-}\frac{u_c^{n+1}-u_c^n}{\Delta t}\,dV = \frac{b}{2}\int_{\mathscr{C}\cap\Omega^-}\nabla\cdot\nabla u_c^{n+1}\,dV + \frac{b}{2}\int_{\mathscr{C}\cap\Omega^-}\nabla\cdot\nabla u_c^{n}\,dV + \int_{\mathscr{C}\cap\Omega^-}\frac{g_c^{n+1}-g_c^n}{2}\,dV. \tag{6}$$

We apply the approximation that u_c^{n+1}, u_c^n, g^{n+1}, and g^n remain constant within the grid cell. The divergence theorem is applied to each Laplacian term in (6),

$$\int_{\mathscr{C}\cap\Omega^-}\nabla\cdot\nabla u_c\,dV = \int_{\partial(\mathscr{C}\cap\Omega^-)}\nabla u_c\cdot n\,dA.$$

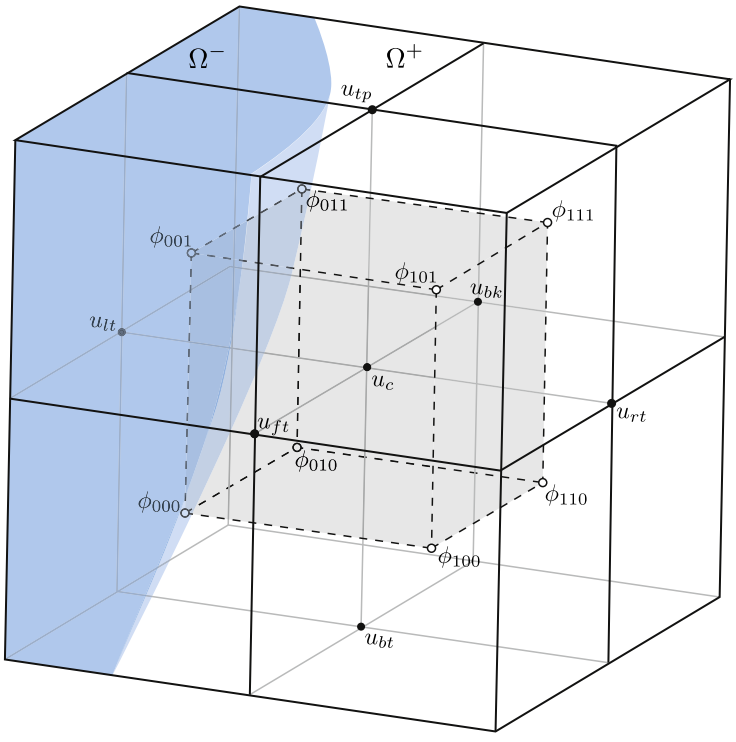

Fig. 3. A fictitious finite volume cell, $\mathscr{C}$ (– – –), within the octree grid near the interface (—).

The integral is split into two components,

$$\int_{\partial(\mathscr{C}\cap\Omega^-)} \nabla u_c \cdot n\, dA = \int_{\partial\mathscr{C}\cap\Omega^-} \nabla u_c \cdot n\, dA + \int_{\Gamma\cap\mathscr{C}} \nabla u_c \cdot n\, dA.$$

The integral over $(\partial\mathscr{C}\cap\Omega^-)$ is performed piecewise over each face of the fictitious cell with standard finite differences for the gradients,

$$\int_{\partial\mathscr{C}\cap\Omega^-} \nabla u_c \cdot n\, dA = \frac{u_{rt}-u_c}{h}A_{+x} + \frac{u_{bk}-u_c}{h}A_{+y} + \frac{u_{tp}-u_c}{h}A_{+z} + \frac{u_{lt}-u_c}{h}A_{-x} + \frac{u_{ft}-u_c}{h}A_{-y} + \frac{u_{bt}-u_c}{h}A_{-z}, \tag{7}$$

where $h=\Delta x=\Delta y=\Delta z$ of $\mathscr{C}$, and $A_{\pm x}$, $A_{\pm y}$, and $A_{\pm z}$ represent the areas of the irregular domain within each face of $\mathscr{C}$.

The evaluation of the integral over $(\Gamma\cap\mathscr{C})$ implicitly imposes the Robin boundary condition (2),

$$\int_{\Gamma\cap\mathscr{C}} \nabla u_c \cdot n\, dA = \int_{\Gamma\cap\mathscr{C}} f\, dA - \alpha u_c A_{\Gamma\cap\mathscr{C}}. \tag{8}$$

The integrals above are calculated with the procedure of Section 2.4.

Remark 1. It is important to note that in the case where the solution is to be solved on both sides of the interface Γ and when the coefficient α is discontinuous, one needs to ensure that the correct value of α is used in the discretization. Consider for example a case where one needs to solve in the interior domain Ω^- where $\alpha=\alpha^-$, then Eq. (8) is to be used for all nodes where $\phi <= 0$ *and* for the nodes adjacent to the interface where $\phi > 0$.

2.4. Cell-based geometric integration

In the evaluation of the line, area, and volume integrals, we utilize a geometric integration method [12,14]. The procedure is to divide each computational cell into a union of simplices S; triangles in two spatial dimensions and tetrahedra in three spatial dimensions. We refer the reader to [12] for further details on the triangulation, since subdivision of the simplices may be required to correctly represent the regions $S\cap\Omega^-$ and $S\cap\Gamma$.

The interface position is linearly interpolated from the level-set values of the vertices of $\mathscr{C}$. Once the triangulation of a cell, $T(\mathscr{C})$, is complete, the integrals are calculated simplex-wise as:

$$\int_{\mathscr{C}\cap\Gamma} f\, d\Gamma = \sum_{S\in T(\mathscr{C})} \int_{S\cap\Gamma} f\, d\Gamma,$$

$$\int_{\mathscr{C}\cap\Omega^-} f\, d\Omega = \sum_{S\in T(\mathscr{C})} \int_{S\cap\Omega^-} f\, d\Omega.$$

A second-order midpoint method is used to calculate the reduced integrals, $\int_{S\cap\Gamma} f\, d\Gamma$ and $\int_{S\cap\Omega^-} f\, d\Omega$.

2.5. Approach for Stefan-type problems

We consider a Stefan-type problem described by Eqs. (1)–(3). The level-set function, ϕ, implicitly defines and captures the evolution of the interface according to the advection equation (4).

Given the solution u^n at time t^n, we use the following algorithm to find a solution to the Stefan problem:

1. Extrapolate the initial temperature field, u^n, over the interface to cover a few grid cells in order to define ghost node values that will be used when assembling the right hand side of the linear system described by (6)–(8) at time t^{n+1}.
2. Calculate the velocity field with (3).
3. Solve the level-set advection equation (4) to obtain the new interface location, ϕ^{n+1}.
4. Reinitialize the level-set function to an approximate signed distance function using the reinitialization scheme in [13].
5. Construct a new quadtree/octree grid from the values of ϕ^{n+1}.
6. Assemble the linear system for the diffusion equation (1) with the discretization procedure of Section 2.3.1.
7. Solve the linear system to find the updated temperature field, u^{n+1}.
8. Repeat from step 1 until the final time is reached.

2.5.1. Extrapolation in the normal direction

In the case of an advancing interface, when assembling the linear system for time t^{n+1}, the values of ρ at time t^n will be needed at grid locations which were outside of the interface at t^n but are swept within the interface from t^n to t^{n+1}. This situation is depicted in Fig. 4. In order to properly define these ghost cell values, we extrapolate the values of the solution from the interior domain over the interface along the normal direction. We use a PDE-based approach for the extrapolation as described in [2]. One can use this approach to extrapolate values over the interface in a constant manner, linearly, or quadratically, depending on the desired accuracy.

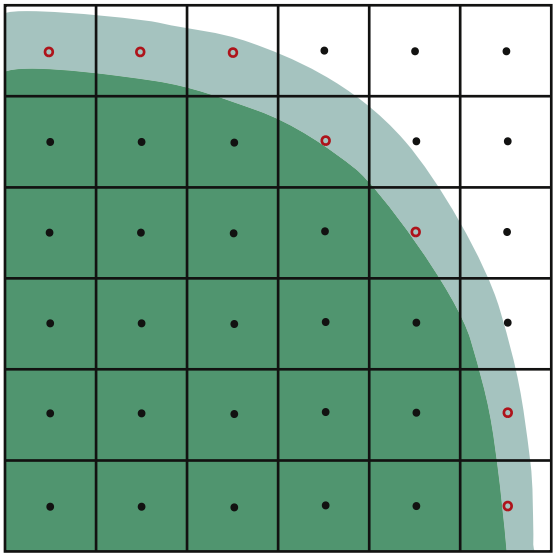

Fig. 4. In the case of an advancing interface, extrapolation in the normal direction is used to define ghost values for the open nodes (shown in red). (For interpretation of the references to color in this figure legend, the reader is referred to the web version of this article.)

The quadratic extrapolation is done in a series of steps. First, the second directional derivative of u in the normal direction is defined only in the interior region Ω^-,

$$u_{nn} = \mathbf{n} \cdot \nabla(\mathbf{n} \cdot \nabla u).$$

Next, this scalar function is extrapolated in a constant manner over the interface by solving for a few time steps:

$$\frac{\partial u_{nn}}{\partial \tau} + H(\phi^n)\mathbf{n} \cdot \nabla u_{nn} = 0,$$

where $H(\phi^n)$ is the Heaviside function which is used to hold in place the known values of u_{nn} in the region $\phi \leqslant 0$. Once the second directional derivative is defined over a band around the interface, we can solve for the first directional derivative, u_n, by solving the PDE,

$$\frac{\partial u_n}{\partial \tau} + H(\phi^n)(\mathbf{n} \cdot \nabla u_n - u_{nn}) = 0,$$

which defines u_n to have a directional derivative equal to u_{nn}. Finally, we solve a similar equation which defines the values of u to have a directional derivative equal to u_n,

$$\frac{\partial u}{\partial \tau} + H(\phi^n)(\mathbf{n} \cdot \nabla u - u_n) = 0.$$

The partial differential equations above are solved over a fictitious time τ, and it is only necessary to iterate a few time steps to obtain extrapolated values of u in a narrow band around the interface.

We utilize central and one-sided differencing in the discretizations for the extrapolation equations. In the case of T-junction nodes, ghost nodes are defined as per the procedures described in Section 2.3.1.

2.5.2. Velocity field calculation

In general, the temperature field must be found in the interior (Ω^-) and exterior (Ω^+) regions separately. We create two copies of the temperature data; a copy of the interior temperature field is extrapolated outward into Ω^+ and a copy of the exterior temperature field is extrapolated inward into Ω^-. We then calculate the jump in u across the interface in a node-by-node manner [9]. Lastly, we perform a constant extrapolation of the calculated velocity in the inward normal direction and in the outward normal direction to define in a narrow band a velocity field that is constant in the normal direction. This produces more numerically accurate results [7,1]. For some examples, the temperature field is a known value in one of the regions, which simplifies the above process considerably.

2.5.3. Level set advection

We use a second-order semi-Lagrangian approach [29] for the level-set advection equation (4). The solution is found by numerically integrating along characteristic curves starting from each grid node, $\mathbf{x}_i$, and tracing back the departure point, $\mathbf{x}_d$, in the upwind direction. In particular, the updated level-set function at a grid node, $\mathbf{x}_i$, is found by

$$\phi^{n+1}(\mathbf{x}_i) = \phi^n(\mathbf{x}_d),$$

where $\mathbf{x}_d$ is the corresponding departure point. We use a second-order trapezoidal method to integrate numerically,

$$\hat{\mathbf{x}} = \mathbf{x}^{n+1} - \Delta t \cdot \mathbf{V}^{n+1}(\mathbf{x}^{n+1}),$$
$$\mathbf{x}_d = \mathbf{x}^{n+1} - \frac{\Delta t}{2} \cdot \mathbf{V}^n(\hat{\mathbf{x}}) - \frac{\Delta t}{2} \cdot \mathbf{V}^{n+1}(\mathbf{x}^{n+1}).$$

The values of $\hat{\mathbf{x}}$ and $\phi^n(\mathbf{x}_d)$ may not be located on a grid node. Non-oscillatory interpolating formulas as described in [13] are used to recover these values.

2.5.4. Reinitialization of the level-set function

At each time step, the level-set function is reinitialized to a signed distance function. We use the reinitialization equation of Sussman et al. [26],

$$\phi_\tau + \mathrm{Sign}(\phi_0)(|\nabla\phi| - 1) = 0,$$

for a few iterations over a fictitious time τ. This equation is discretized with a Godunov approach on adaptive grids as described in [13].

2.5.5. Remeshing

After each time step, the mesh is automatically regenerated to retain the structure defined in Section 2.2, namely the uniform band of cells near the interface and the finest grid cells near the interface. A new grid is defined based on the updated level-set function, ϕ^{n+1}. The nodal values of the solution are interpolated from the previous grid locations with a non-oscillatory quadratic method as described in [13].

2.5.6. Solving the linear system

The linear system is nonsymmetric due to the discretization at T-junction nodes. In our examples, we utilize a biconjugate gradient stabilized method (BiCGSTAB) with a symmetric Gauss–Seidel preconditioner. While a symmetric linear system is usually preferred to a nonsymmetric one in terms of robustness, the overall computational cost is greatly reduced with non-uniform grids since there are far fewer grid nodes.

3. Examples

We provide a set of numerical examples that suggest that the solution is second-order accurate in both the L^1 and L^∞ norms. We also provide some comparisons with uniform grids to demonstrate the improvement in computational efficiency.

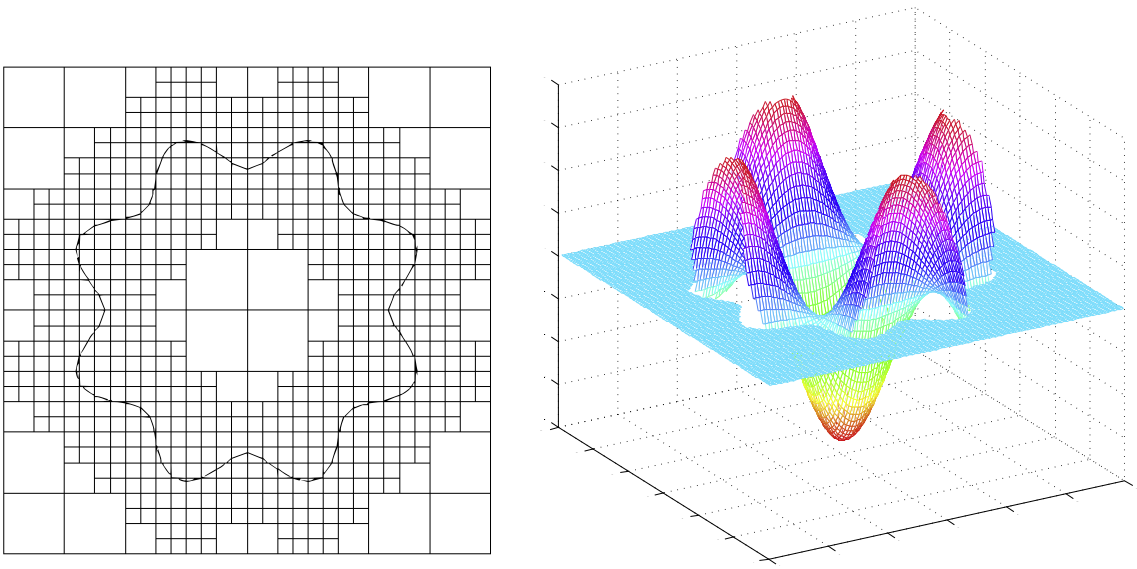

Fig. 5. Left: an illustration of the quadtree mesh over the irregular domain of Examples 1 and 2. This mesh has a maximum resolution of min $\mathrm{level} = 3$ and max $\mathrm{level} = 5$. Right: the solution at time $t = 0.5$.

3.1. Diffusion in two spatial dimensions

Example 1. The first validation example is a diffusion problem in two spatial dimensions over the irregular domain given by the zero isocontour of $\phi = 0.4\cos(8\theta) + \sqrt{x^2+y^2} - \pi$, where $\theta \in [0, 2\pi]$, as illustrated in Fig. 5. The quadtree grid is constructed over the domain, $\Omega = [-1.5\pi, 1.5\pi] \times [-1.5\pi, 1.5\pi]$. The analytical solution is given by $u = -e^{-2t}\cos x \cos y$, and the boundary condition (2) is formulated with $\alpha = 1$. The diffusion equation is solved from time $t = 0$ to $t = 1$, and the convergence rates are presented in Figs. 6 and 7. The quadtree grid is defined with a resolution of min level $= 3$ and max level $= 5$. It is subsequently refined with resolutions of $(\min \text{ level}, \max \text{ level}) = (4,6), (5,7), (6,8)$, and $(7,9)$. The solution is second-order accurate in the L^1 and L^∞ norms.

Example 2. A second example for the diffusion equation in two spatial dimensions is presented over a star-shaped domain given by the zero isocontour of $\phi = r - 0.5 - (y^5 + 5x^4y - 10x^2y^3)/(6r^5)$, where $r = \sqrt{x^2+y^2}$, which is illustrated in Fig. 8. The quadtree grid is constructed over the domain, $\Omega = [-1,1] \times [-1,1]$. The analytical solution is given by $u = -e^{-2t}\cos x \cos y$, and the boundary condition is formulated with $\alpha = 1$. The diffusion equation is solved from time $t = 0$ to $t = 1$, and the convergence rates are presented in Figs. 9 and 10. The quadtree grid is defined with resolutions of $(\min \text{ level}, \max \text{ level}) = (3,7), (4,8)$, and $(5,9)$. The solution is second-order accurate in the L^1 and L^∞ norms.

3.2. Stefan-type problem in two spatial dimensions

Example 3. The Frank sphere problem [8] describes the transition of a supercooled liquid into a solid phase. This problem provides an analytical solution to a Stefan problem. The solid grows radially outward from the origin as a cylinder in two spatial dimensions under a temperature field governed by Eq. (1) with $b = 1$ and $g = 0$.

The classical problem prescribes a Dirichlet boundary condition at the interface. We have reformulated the boundary condition to a Robin type given by Eq. (2), with $\alpha = 1$ and

$$f(s,t) = \frac{2u_\infty}{\mathrm{E}_1\left(\frac{S_o^2}{4}\right)} t^{-\frac{1}{2}} s^{-1} e^{-\frac{s^2}{4}} + u_\infty \left(1 - \frac{\mathrm{E}_1\left(\frac{s^2}{4}\right)}{\mathrm{E}_1\left(\frac{S_o^2}{4}\right)}\right),$$

where $s = r \cdot t^{-1/2}$ is a similarity variable, and S_o represents the initial radius of the solid crystal. The temperature field, u, is zero within the solid region, represented by Ω^+, and is given by the following exact solution within the liquid region, represented by Ω^-,

$$u(s) = u_\infty \left(1 - \frac{\mathrm{E}_1\left(\frac{s^2}{4}\right)}{\mathrm{E}_1\left(\frac{S_o^2}{4}\right)}\right).$$

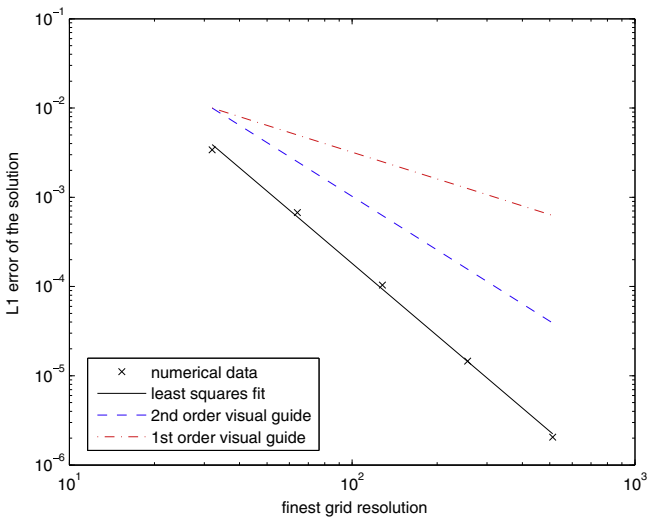

Fig. 6. Accuracy results in the L^1 norm for the diffusion problem in two spatial dimensions of Example 1.

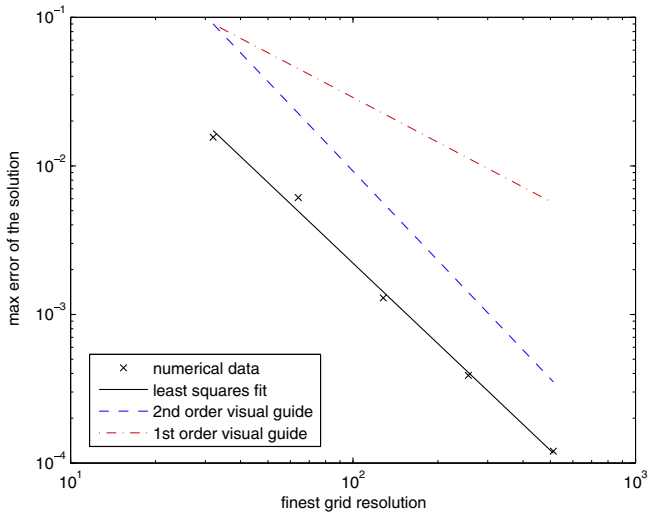

Fig. 7. Accuracy results in the L^∞ norm for the diffusion problem in two spatial dimensions of Example 1.

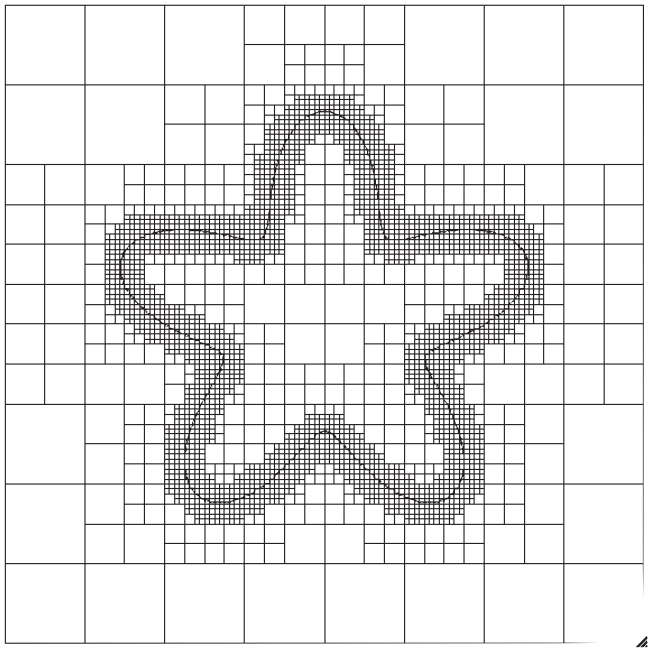

Fig. 8. An illustration of the quadtree mesh over the irregular domain of Example 2. This mesh has a min level = 3 and max level = 7.

The simulation is taken over the computational domain, $\Omega = [-3,3] \times [-3,3]$. The initial radius is taken as $R_o = 0.75$ and the far field temperature value is taken as $u_\infty = -.246$. The simulation was performed from the initial time $t = 1$ to the final time $t = 2$. The accuracy results of the temperature field are presented in Figs. 11 and 12. The accuracy of the radius location is presented in Figs. 13 and 14. These simulations were done with adaptive grids at the resolutions (min level, max level) = (3,5), (4,6), (5,7), (6,8), and $(7,9)$. The numerical solutions are first-order accurate in the L^1 and L^∞ norms, which is to be expected since the evolution is dependent upon the gradient of the temperature field. A plot illustrating the evolution of the phase boundary is presented in Fig. 15 for times of $t = 1$, $t = 1.25$, $t = 1.5$, and $t = 1.75$.

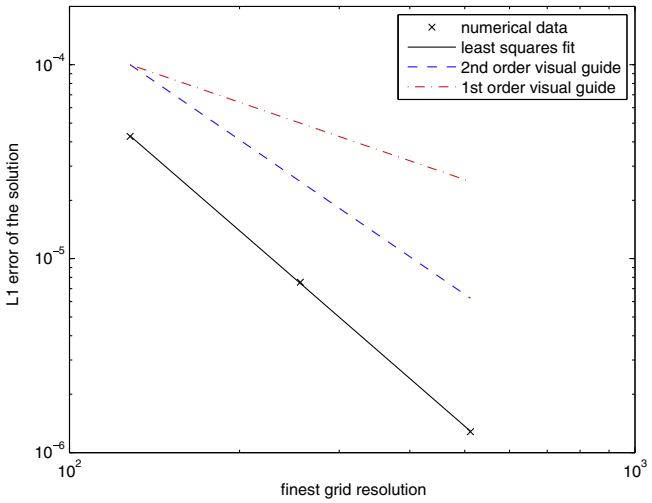

Fig. 9. Accuracy results in the L^1 norm for the diffusion problem in two spatial dimensions of Example 2.

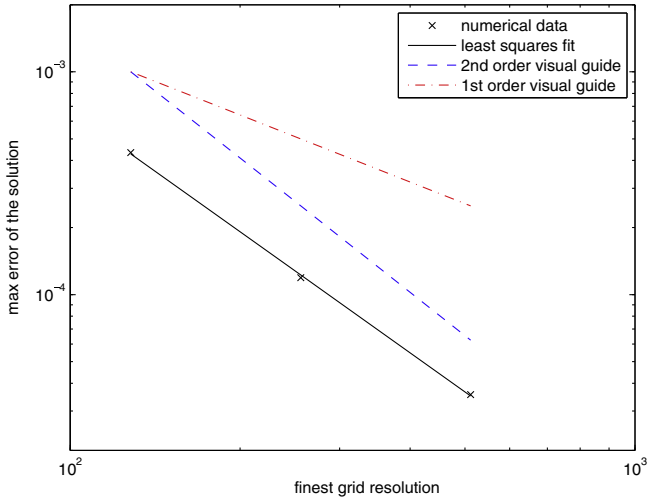

Fig. 10. Accuracy results in the L^∞ norm for the diffusion problem in two spatial dimensions of Example 2.

3.3. Diffusion problem in three spatial dimensions

Example 4. A diffusion problem in three spatial dimensions is given by Eq. (1) with $b = 1$ and $g = 0$ over a stationary sphere of radius $r = 0.55$ centered at the origin. The computational domain is taken as $\Omega = [-1,1] \times [-1,1] \times [-1,1]$. The boundary condition is given by (2) with $\alpha = 1$ and

$$f = e^{-t}(x/r \cdot \cos x - y/r \cdot \sin y - z/r \cdot \sin z + \sin x + \cos y + \cos z).$$

The simulation was performed over the time interval $t = 0$ to $t = 1$. The exact solution to this problem is given by $u = e^{-t}(\sin x + \cos y + \cos z)$.

The accuracy results are presented in Figs. 17 and 18 for uniform grids and in Figs. 19 and 20 for nonuniform octree grids. Resolutions of 16^3, 32^3, 64^3, and 128^3 were used with uniform grids and resolutions of $(3,5)$, $(4,6)$, and $(5,7)$ were used in the nonuniform simulations. The numerical solutions are second-order accurate in the L^1 and L^∞ norms. Fig. 16 illustrates a typical octree mesh.

There is a considerable savings of computational resources when utilizing octree grids. For example, we achieved a similar level of accuracy for the solution with a 128^3 uniform grid and a $(\text{min res.} = 16, \text{max res.} = 128)$ nonuniform grid. The

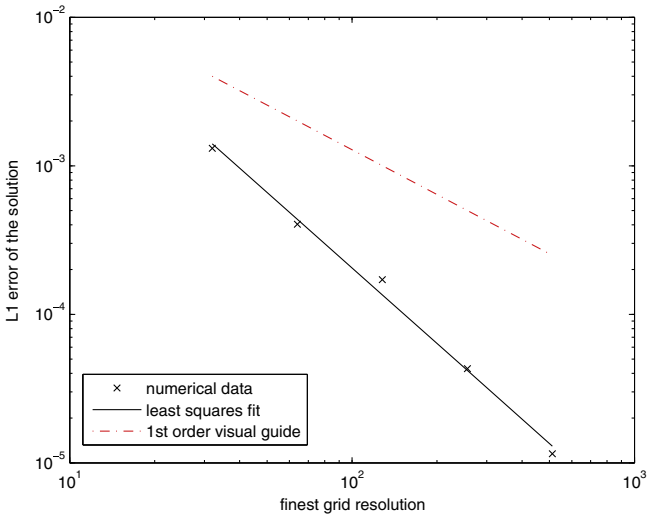

Fig. 11. Accuracy results in the L^1 norm for the temperature field of the Frank sphere problem in two spatial dimensions of Example 3.

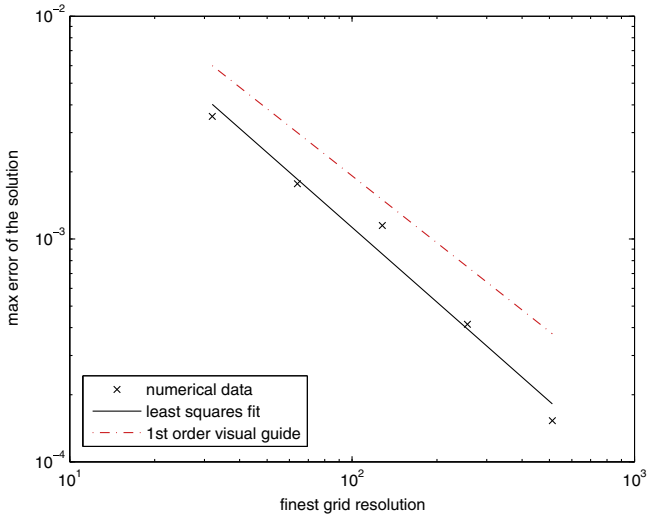

Fig. 12. Accuracy results in the L^∞ norm for the temperature field of the Frank sphere problem in two spatial dimensions of Example 3.

number of grid nodes in each simulation differs by almost an order of magnitude: 2,146,689 and 265,913, respectively, while the numerical errors in the L^∞ norm are similar ($2.61e^{-4}$ versus $2.58e^{-4}$).

3.4. Moving-boundary problems in three spatial dimensions

Example 5. The Frank sphere problem in three spatial dimensions describes the phase growth of a solid sphere in a supercooled liquid and provides an analytical solution to a Stefan-type problem. The temperature field is governed by the diffusion equation (1) with $b = 1$ and $g = 0$. The velocity field is calculated with Eq. (3) with $D = 1$.

The analytical solution for the temperature field in the liquid phase is given by

$$u(s) = A(s^{-1}e^{-s^2/4} - \pi^{1/2}/2(1 - \mathrm{erf}(s/2))) + T_\infty,$$

where s is a similarity variable defined by $s = rt^{-1/2}$, and $A = 0.5S_o^3 e^{-S_o^2/4}$. The temperature in the solid phase is zero.

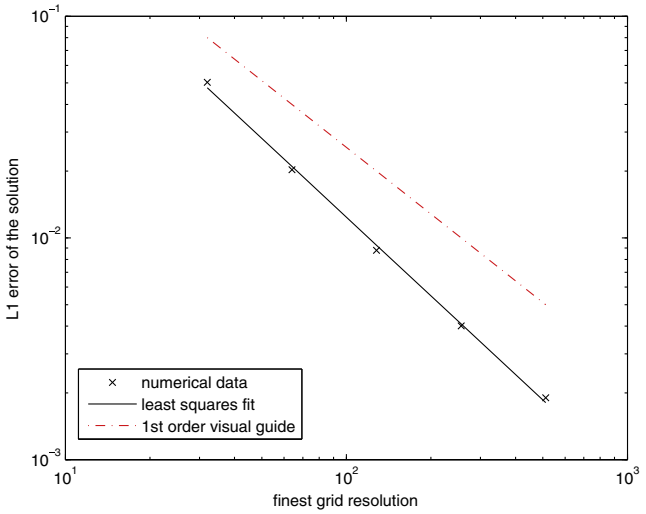

Fig. 13. Accuracy results in the L^1 norm for the phase boundary location of the Frank sphere problem in two spatial dimensions of Example 3.

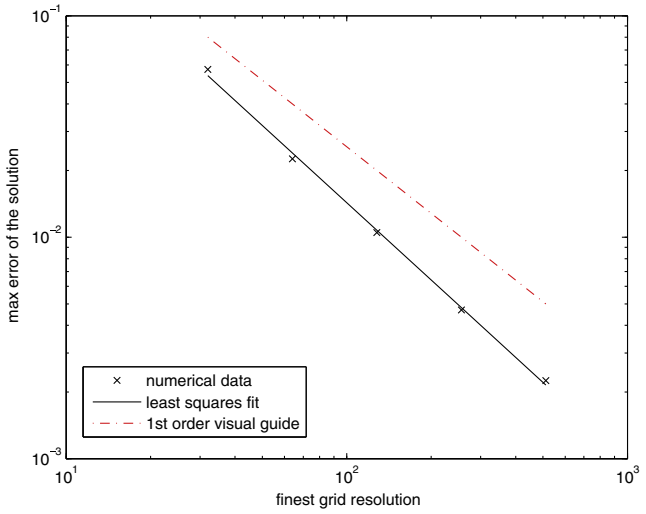

Fig. 14. Accuracy results in the L^∞ norm for the phase boundary location of the Frank sphere problem in two spatial dimensions of Example 3.

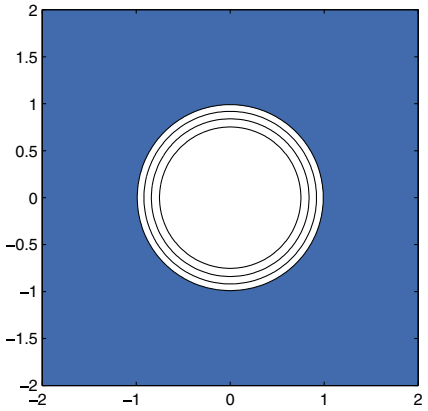

Fig. 15. The evolution of the phase boundary in the Frank sphere problem in two spatial dimensions. The boundary is displayed at times of $t = 1$, $t = 1.25$, $t = 1.5$, and $t = 1.75$.

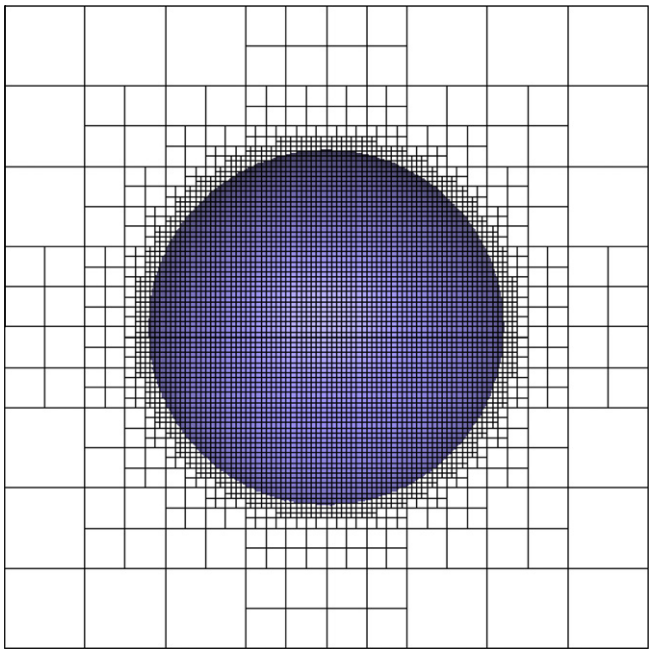

Fig. 16. An example of a typical octree grid for the diffusion problem over a sphere of Example 4.

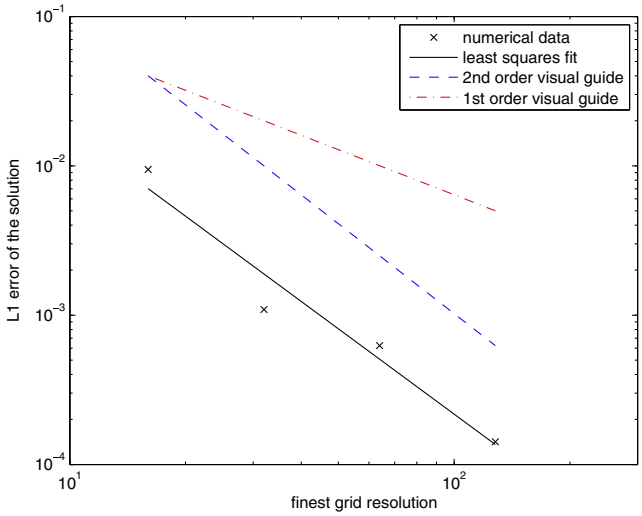

Fig. 17. Accuracy results in the L^1 norm for the diffusion problem in three spatial dimensions of Example 4 on uniform grids.

We have run the simulation over the domain $[-3,3] \times [-3,3] \times [-3,3]$. The initial radius of the sphere is taken as $r_o = 1$. The simulation is run from a time of $t = 1$ to $t = 2$. The computational domain and octree grid is displayed in Fig. 21 for the initial and final times of the simulation. The accuracy results of the interface evolution are presented in Figs. 23 and 24 over adaptive grids with resolutions of $(2,4)$, $(3,5)$, and $(4,6)$. The numerical results are first-order accurate. Fig. 22 illustrates the temperature profile of the $z = 0$ cross section of the domain at the final time of $t = 2$. The plot is generated from interpolated values of a $(\text{min res.} = 8, \text{max res.} = 64)$ grid.

3.5. Simulation of epitaxial growth with an Ehrlich–Schwoebel barrier

Epitaxial growth is an example of modern computational science where a Robin boundary condition plays an important role. Epitaxy is the preferred method to grow semiconductors, layer by layer: atoms are deposited on the flat substrate and

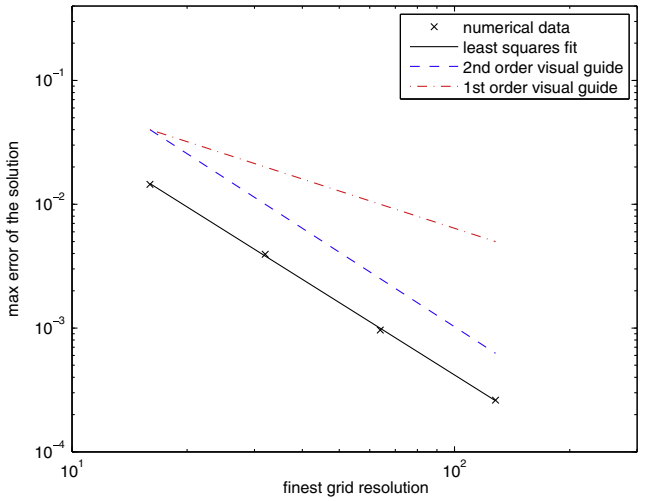

Fig. 18. Accuracy results in the L^∞ norm for the diffusion problem in three spatial dimensions of Example 4 on uniform grids.

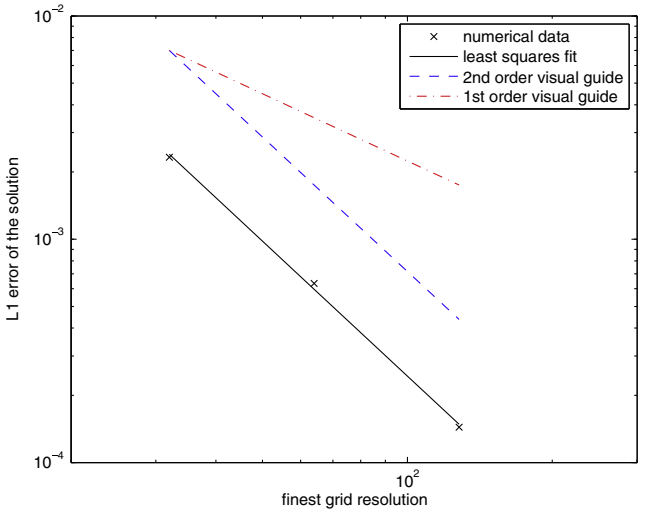

Fig. 19. Accuracy results in the L^1 norm for the diffusion problem in three spatial dimensions of Example 4 on nonuniform octree grids.

subsequently diffuse until they nucleate to form dimers. Further attachment of adatoms contributes to the growth of existing islands and can result in desired nanostructures. A continuum model, the island dynamics model, was introduced by Caflisch et al. [4] to describe the diffusion of adatoms that are deposited on a substrate, their nucleations and the subsequent growth of islands. The model employs coarse-graining in the lateral directions, but retains atomistic discreteness in the growth directions. This is achieved through a level-set approach in which islands of height $k+1$ are described by the kth isocontour of the level-set function, ϕ, which is evolved according to

$$\phi_t + v_n|\nabla\phi| = 0, \tag{9}$$

where v_n is the normal velocity of the islands' boundaries. This velocity is obtained from solving the diffusion equation for the adatom concentration $\rho(\mathbf{x}, t)$:

$$\frac{\partial\rho}{\partial t} = F + D\nabla^2\rho - 2\frac{dN}{dt}, \quad \rho(t=0) = 0. \tag{10}$$

In Eq. (10), D is the surface diffusion coefficient, F is the depositon flux, and dN/dt is the nucleation rate. Once the adatom concentration has been found, the velocity is computed by balancing the flux of adatoms at the boundaries of the islands,

$$v_n = a^2 D(\mathbf{n}\cdot\nabla\rho^- - \mathbf{n}\cdot\nabla\rho^+), \tag{11}$$

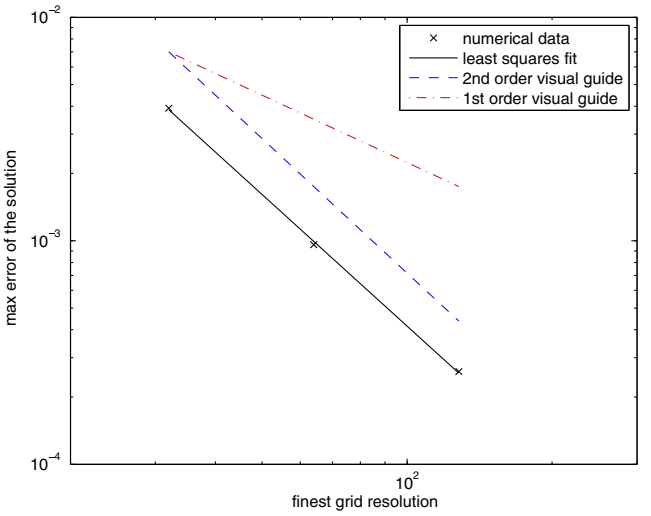

Fig. 20. Accuracy results in the L^{∞} norm for the diffusion problem in three spatial dimensions of Example 4 on nonuniform octree grids.

where the subscripts refer to the fluxes of adatoms from the terraces above (+) and below (−) the island edge.

The presence of an Ehrlich–Schwoebel barrier at the step edges results in a Robin boundary condition for the diffusion equation as detailed in [20]. Consider for example a step edge barrier in one dimension as illustrated in Fig. 25. The diffusion rates D, D', and D'' represent the rates of diffusion along the terrace (D), toward the step edge from the upper terrace (D'), and toward the step edge from the lower terrace (D''). First, consider the adatoms migrating to the step edge from the upper terrace. The adatom density on the upper terrace at one atomic distance from the step edge is given by $\rho(x_n - a)$. Due to the step edge barrier, the quantity of atoms that stick to the step per unit time and length is given by $D'\rho(x_n - a)/a$, where D' is the rate of diffusion over a step edge (toward the lower terrace). The number of atoms detaching from the step and going to the upper terrace is given by $D'\rho_{eq}/a$, where ρ_{eq} is the equilibrium adatom density at the step edge. The macroscopic flux of adatoms leaving the upper terrace is given by $-D(\nabla\rho \cdot n)$, where D is rate of diffusion for atoms diffusing on the terrace away from the step edge. The boundary condition for balancing the current of adatoms at the upper side of the step is given by,

$$D\frac{\partial\rho}{\partial n}(x_n) = D'(\rho_{eq} - \rho(x_n - a))/a \approx D'(\rho_{eq} - \rho(x_n))/a + D'\frac{\partial\rho}{\partial n}(x_n).$$

Rearranging terms, this boundary condition simplifies to

$$\nabla\rho \cdot \mathbf{n} = \frac{D'}{D - D'}(\rho_{eq} - \rho).$$

Similarly, when we consider the interaction between the adatoms on the lower terrace and the step edge, the balance of flux yields the following boundary condition,

$$\nabla\rho \cdot \mathbf{n} = \frac{D''}{D - D''}(\rho_{eq} - \rho).$$

This example is provided to show the effect of the step edge barrier on the adatom concentration. The simulation begins with a concentric stack of islands of radii 1/3 and 1/9 of the domain length, resembling a wedding cake as shown in Fig. 26. The initial adatom concentration is zero everywhere in the domain. At time $t = 0$, a flux of adatoms is deposited onto the structure. Several simulations are run in which the strength of the step edge barrier on the upper terraces, determined by the parameter D'/D, is varied. The strength of the step edge barrier on the lower terraces is held at a constant ratio of $D''/D = 0.99$, which corresponds to negligible barrier strength. In order to study the evolution of the adatom density, nucleation of new islands has been prevented in these simulations.

The effect of a strong barrier ($D'/D = 10^{-6}$) versus a negligable barrier ($D'/D = 0.99$) is given in Figs. 27 and 28. In the case of a large barrier, the Robin boundary condition reduces to $\frac{\partial\rho}{\partial n} = 0$, hence a flat profile, which is illustrated in Fig. 27. We can also observe that the concentration of adatoms on the upper terrace is equal to the total amount of flux deposited, $5e^{-3}$. This behavior is physically correct since such a large barrier would prevent adatoms from migrating down to the lower terrace. In contrast, in the case where the barrier is negligible ($D'/D = 0.99$), the Robin boundary condition reduces to $\rho_{\Gamma} \to \rho_f$, where ρ_f is the equilibrium adatom density, taken as $\rho_f = 1e^{-3}$. Fig. 28 clearly demonstrates that our approach is able to simulate this case as well.

It is also interesting to note the influence of the value of D'/D away from those two extremes. Figs. 29–31 give the density profiles for intermediate barrier strengths. We can note that the profiles are similar in nature, but the peak value of ρ is larger

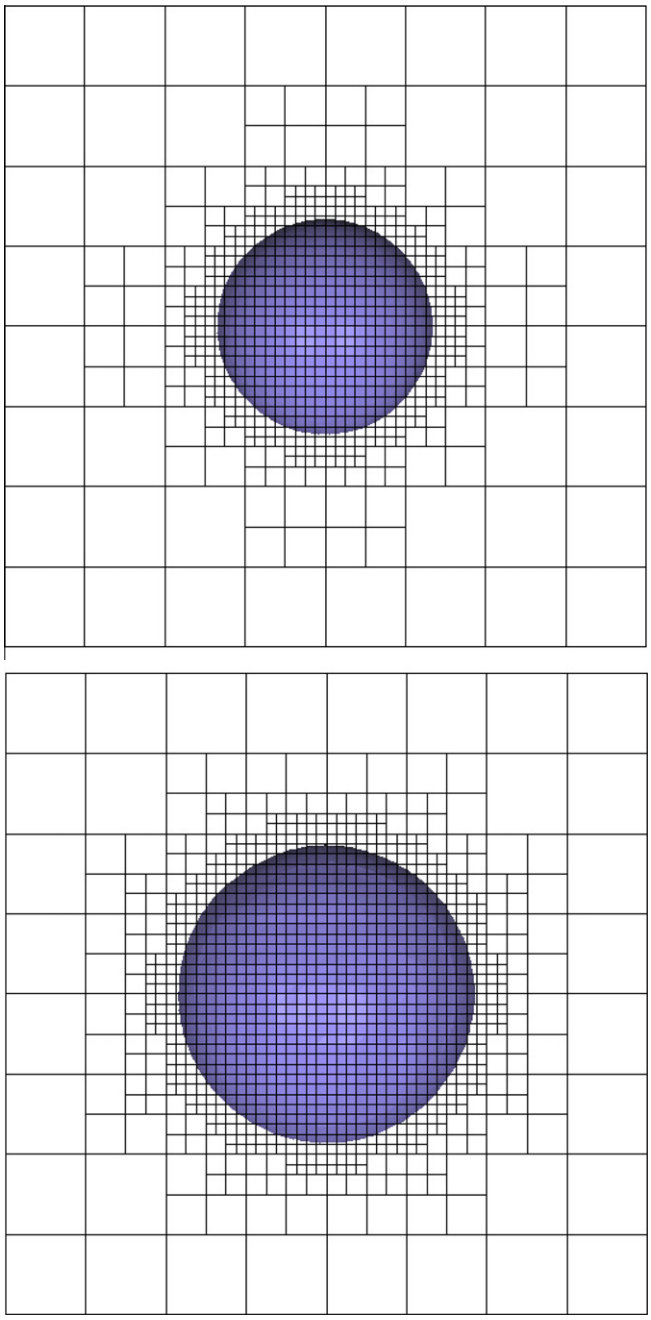

Fig. 21. The computational domain for the Frank sphere problem in three spatial dimensions on an adaptive octree grid. The initial crystal (upper) grows spherically outward to the final state at $t = 2$ (lower).

for lower values of D'/D. In turn, this will translate into higher nucleation rates and the well-known mounding observed in epitaxial growth [27,16]. For all of these simulations, we have used a diffusion rate of $D/F = 10^6$ and a system size of $L = 90$ atoms. We have chosen a very short simulation time of 0.005 in order to clearly demonstrate the changes in the adatom density profile. Because of this the islands grow very little. We note, however that the approach works correctly for much longer simulations.

3.5.1. Grid anisotropy

There exists a morphological instability that can arise in epitaxial growth with a step-edge barrier [3]. The physics of the instablility are qualitatively similar to the physics of dendritic growth. This is an important phenomenon that may be applied

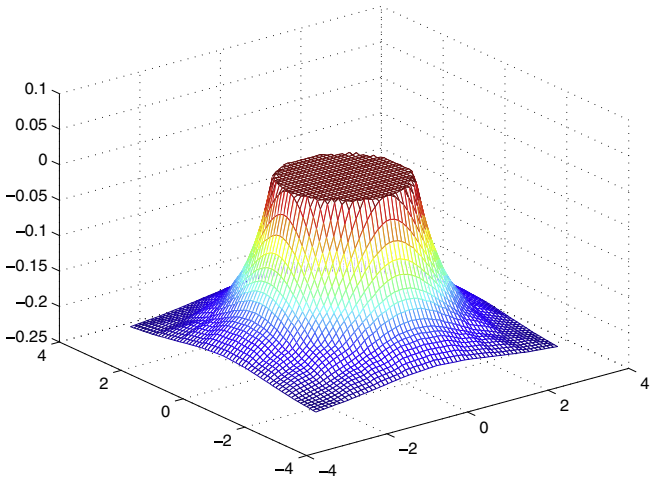

Fig. 22. The temperature profile of the $z = 0$ cross section after growth from $t = 1$ to $t = 2$ of the Frank sphere problem in three spatial dimensions.

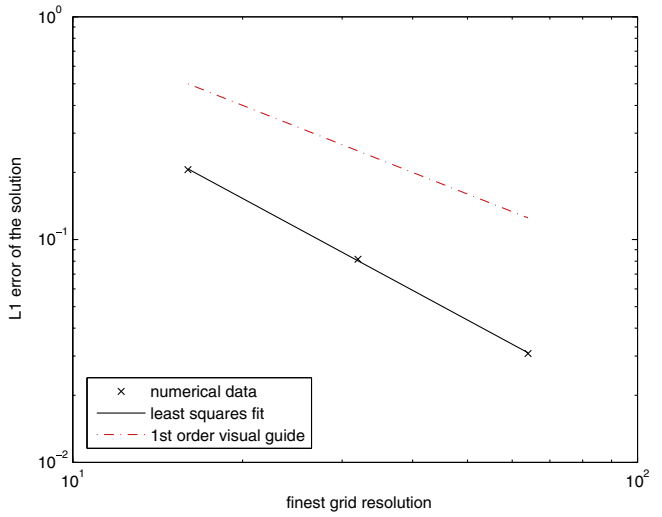

Fig. 23. Accuracy results in the L^1 norm for the phase boundary location of the Frank sphere problem in three spatial dimensions of Example 5.

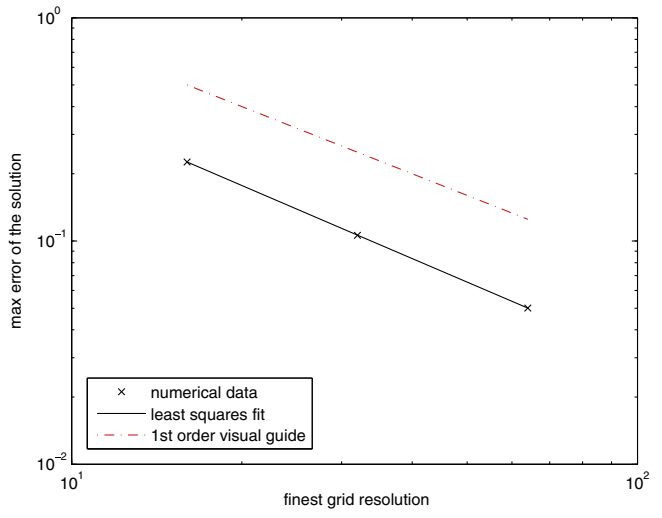

Fig. 24. Accuracy results in the L^∞ norm for the phase boundary location of the Frank sphere problem in three spatial dimensions of Example 5.

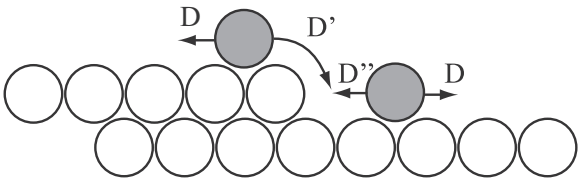

Fig. 25. Schematic of a step-edge barrier in one dimension [20]. The rates D, D', and D'' represent the rate of diffusion along the terrace, toward the step edge from the upper terrace, and towards the step edge from the lower terrace.

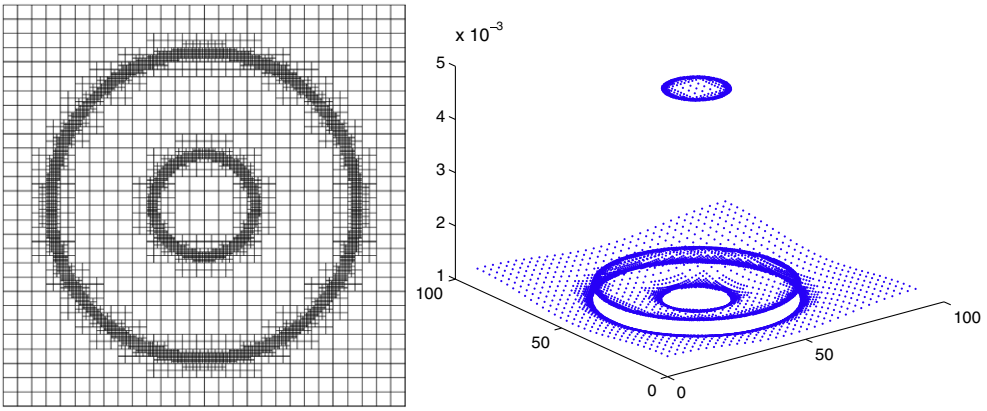

Fig. 26. Geometry and computational mesh for the island dynamics test problem (left). A grid node plot of the adatom density is shown on the right.

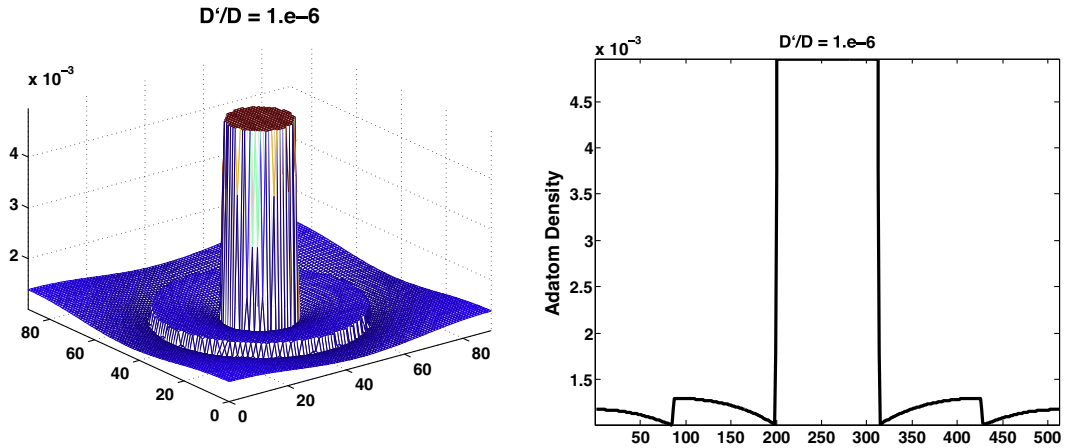

Fig. 27. Mesh plot (left) and centerline profile plot (right) of the adatom density with an upper barrier strength of $D'/D = 1e^{-6}$.

to nanoscale shape control [10]. The following example exhibits this Bales–Zangwill instability for the growth of a single island. It is provided as a test of the amount of grid anisotropy produced by this numerical approach.

The initial shape of the island is a circle which has been perturbed by a sinusoid along the interface. The level set function is given by $\phi = 0.004d\cos(8\theta) + \sqrt{x^2 + y^2} - 0.125d$, where d is the domain length. The simulation parameters are $D/F = 10^8$, $D'/D = 0.01$, $D''/D = 0.99$, $\rho_f = 10^{-3}$, and $L = 90$. In order to provide a symmetric diffusion field, a Dirichlet boundary condition, $\rho = \rho_f$, is applied to a large circle at the boundary of the Cartesian domain. Fig. 32 is a plot of the interface as it grows up to a time of $t = 0.32$ on an adaptive grid with a resolution of min level = 5 and max level = 8. We observe a small amount of grid anisotropy. We attribute this to the use of finite differences on the Cartesian grid; specifically the gradients of the adatom density used in the velocity calculation are decomposed into x and y components.

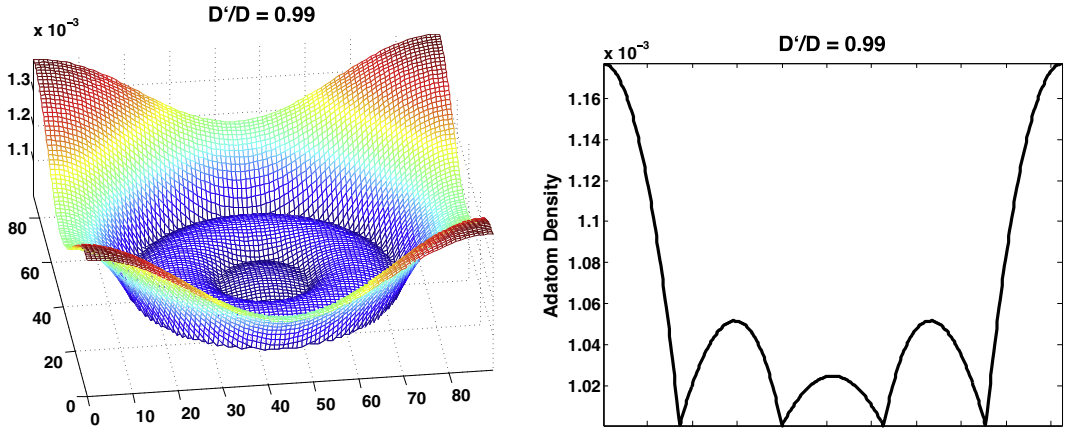

Fig. 28. Mesh plot (left) and centerline profile plot (right) of the adatom density with an upper barrier strength of $D'/D = 0.99$.

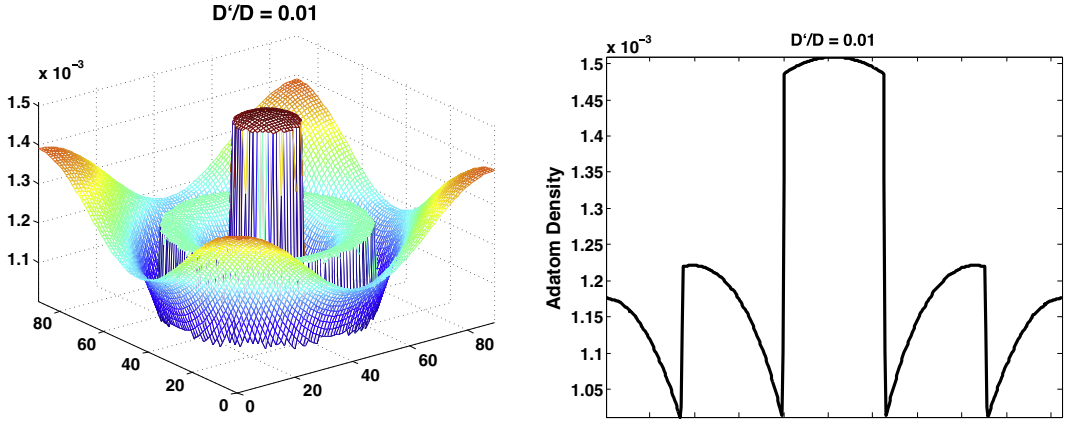

Fig. 29. Mesh plot (left) and centerline profile plot (right) of the adatom density with an upper barrier strength of $D'/D = 0.01$.

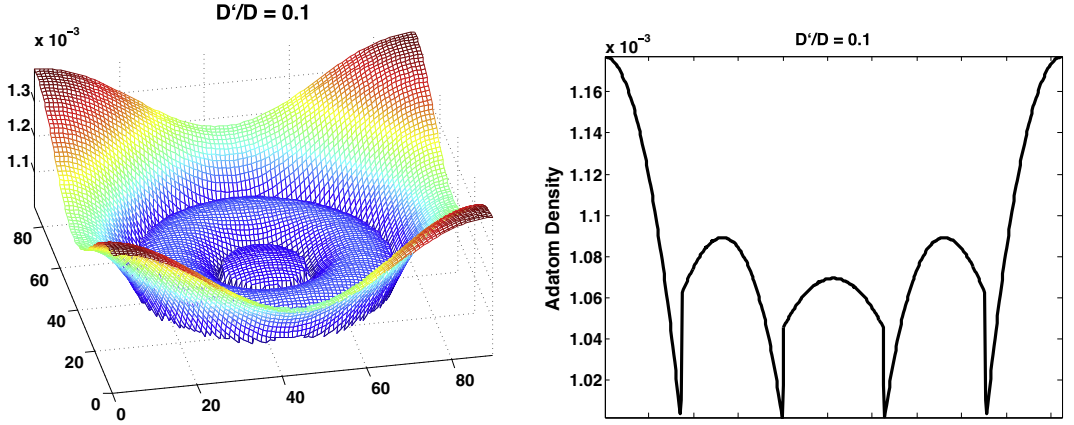

Fig. 30. Mesh plot (left) and centerline profile plot (right) of the adatom density with an upper barrier strength of $D'/D = 0.1$.

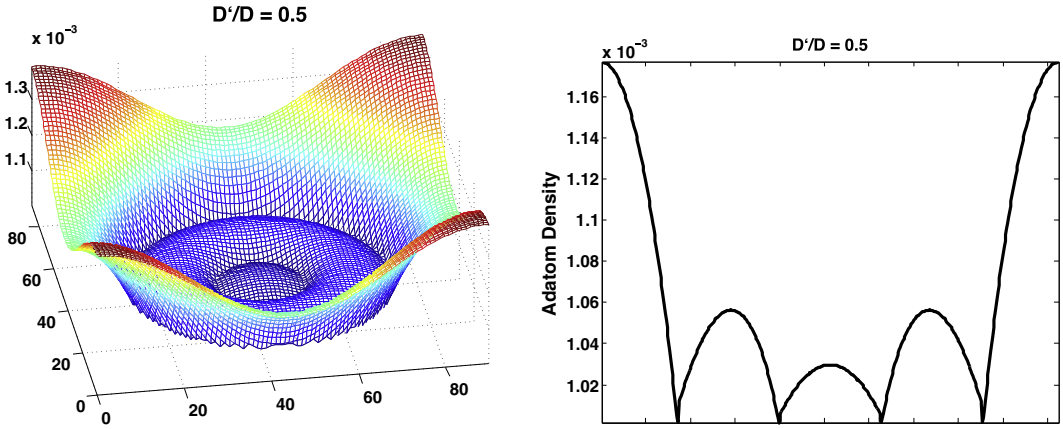

Fig. 31. Mesh plot (left) and centerline profile plot (right) of the adatom density with an upper barrier strength of $D'/D = 0.5$.

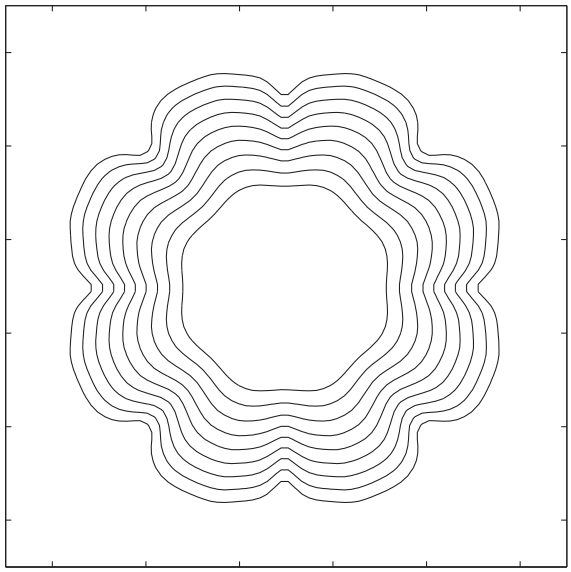

Fig. 32. The unstable growth of a single island indicates a small amount of grid anisotropy.

4. Conclusions

We have presented a numerical approach for the diffusion equation on irregular domains and Stefan-type problems with Robin boundary conditions on adaptive Cartesian grids. The discretization is straightforward to implement, and even though the resulting linear system is nonsymmetric, it results in a diagonally dominant M-matrix and thus can be solved efficiently. In this work, we have used BiCGSTAB but it is clear that multigrid methods would further improve the efficiency. We have demonstrated second-order accurate solutions to the diffusion equation and first-order accurate solutions for Stefan-type problems in two and three spatial dimensions in the L^∞ norm. The approach is robust and is shown to be significantly more efficient than similar methods on uniform grids. We applied the numerical approach to a simulation of epitaxial growth with an Ehrlich–Schwoebel step edge barrier and have found qualitative agreement with the expected physical behavior.

Acknowledgement

This material is based upon work supported by the National Science Foundation under grant agreement CHE 1027797 and CHE 1027817. The research of F. Gibou was also supported in part by ONR under grant agreement N00014-11-1-0027, by the Institute for Collaborative Biotechnologies through contract No. W911NF-09-D-0001 from the U.S. Army Research Office and by the W.M. Keck Foundation.

References

[1] D. Adalsteinsson, J. Sethian, A fast level set method for propagating interfaces, J. Comput. Phys. 118 (1995) 269–277.
[2] T. Aslam, A partial differential equation approach to multidimensional extrapolation, J. Comput. Phys. 193 (2004) 349–355.
[3] G.S. Bales, A. Zangwill, Morphological instability of a terrace edge during step-flow growth, Phys. Rev. B 41 (1990) 5500–5508.
[4] R. Caflisch, M. Gyure, B. Merriman, S. Osher, C. Ratsch, D. Vvedensky, J. Zinck, Island dynamics and the level set method for epitaxial growth, Appl. Math. Lett. 12 (1999) 13.
[5] H. Chen, C. Min, F. Gibou, A supra-convergent finite difference scheme for the Poisson and heat equations on irregular domains and non-graded adaptive Cartesian grids, J. Sci. Comput. 31 (2007) 19–60.
[6] H. Chen, C. Min, F. Gibou, A numerical scheme for the Stefan problem on adaptive Cartesian grids with supralinear convergence rate, J. Comput. Phys. 228 (2009) 5803–5818.
[7] S. Chen, B. Merriman, S. Osher, P. Smereka, A simple level set method for solving Stefan problems, J. Comput. Phys. 135 (1997) 8–29.
[8] F. Frank, Radially symmetric phase growth controlled by diffusion, Proc. R. Soc. A 201 (1950) 586.
[9] F. Gibou, R. Fedkiw, R. Caflisch, S. Osher, A level set approach for the numerical simulation of dendritic growth, J. Sci. Comput. 19 (2003) 183–199.
[10] Zhengzheng Hu, Shuwang Li, John S. Lowengrub, Morphological stability analysis of the epitaxial growth of a circular island: application to nanoscale shape control, Physica D: Nonlinear Phenom. 233 (2) (2007) 151–166.
[11] F.P. Incropera, D.P. DeWitt, Fundamentals of Heat and Mass Transfer, John Wiley, 2007.
[12] C. Min, F. Gibou, Geometric integration over irregular domains with application to level set methods, J. Comput. Phys. 226 (2007) 1432–1443.
[13] C. Min, F. Gibou, A second order accurate level set method on non-graded adaptive Cartesian grids, J. Comput. Phys. 225 (2007) 300–321.
[14] C. Min, F. Gibou, Robust second order accurate discretization of the multi-dimensional Heaviside and Dirac delta functions, J. Comput. Phys. 227 (2008) 9686–9695.
[15] Y.T. Ng, C. Min, F. Gibou, Efficient fluid-solid coupling for one phase flows, J. Comput. Phys. 228 (2009) 8807–8829.
[16] C. Orme, M.D. Johnson, J.L. Sudijono, K.T. Leung, B.G. Orr, Large scale surface structure formed during GaAs(001) homoepitaxy, Appl. Phys. Lett. 64 (7) (1994) 860–862.
[17] S. Osher, R. Fedkiw, Level Set Methods and Dynamic Implicit Surfaces, Springer-Verlag, New York, NY, 2002.
[18] S. Osher, J. Sethian, Fronts propagating with curvature-dependent speed: algorithms based on Hamilton–Jacobi formulations, J. Comput. Phys. 79 (1988) 12–49.
[19] J. Papac, F. Gibou, C. Ratsch, Efficient symmetric discretization for the Poisson, heat and Stefan-type problems with Robin boundary conditions, J. Comput. Phys. 229 (2010) 875–889.
[20] A. Pimpinelli, J. Villain, Physics of Crystal Growth, Cambridge University Press, 1998.
[21] B.W. Pogue, S. Geimer, T.O. McBride, S. Jiang, U.L. Osterberg, K.D. Paulsen, Three-dimensional simulation of near-infrared diffusion in tissue: boundary condition and geometry analysis for finite-element image reconstruction, Appl. Opt. 40 (2001) 588–600.
[22] J.W. Purvis, J.E. Burkhalter, Prediction of critical Mach number for store configurations, AIAA J. 17 (1979) 1170–1177.
[23] H. Samet, The Design and Analysis of Spatial Data Structures, Addison-Wesley, New York, 1989.
[24] H. Samet, Applications of Spatial Data Structures: Computer Graphics, Image Processing and GIS, Addison-Wesley, New York, 1990.
[25] J.A. Sethian, Level Set Methods and Fast Marching Methods, Cambridge University Press, Cambridge, 1999.
[26] M. Sussman, P. Smereka, S. Osher, A level set approach for computing solutions to incompressible two-phase flow, J. Comput. Phys. 114 (1994) 146–159.
[27] Joseph E. Van Nostrand, S. Jay Chey, M.A. Hasan, David G. Cahill, J.E. Greene, Surface morphology during multilayer epitaxial growth of Ge(001), Phys. Rev. Lett. 74 (1995) 1127–1130.
[28] J. Villain, Continuum models for crystal growth from atomic beams with and without desorption, J. Phys. 1 (1991) 19.
[29] D. Xiu, G. Karniadakis, A semi-Lagrangian high-order method for Navier–Stokes equations, J. Comput. Phys. 172 (2001) 658–684.